

# Development of a Penguin-Inspired Swimming Robot With Air Lubrication System

Jie Pan , Ziye Zhou , Jian Wang , *Member, IEEE*, Pengfei Zhang , and Junzhi Yu , *Fellow, IEEE*

**Abstract**—In this article, a novel robotic penguin equipped with air lubrication system is developed. Through mimicking the agile movements of biological penguins, two degrees of freedom (DOF) wings including heaving and pitching motions, and a buoyancy-driven system for ascending and diving are particularly designed. Meanwhile, a complete 3-D dynamic model is established based on the Morrison equation, and the hydrodynamic parameters are determined with experimental results. Then, taking the bioinspired central pattern generators as the main actuation, the 3-D locomotion performance is discussed. More importantly, inspired by the leaping behavior of penguins, a unique air lubrication system is developed, and the obtained results verify the effectiveness of the mechatronic design. This work will offer valuable insight into the future development and control of next-generation versatile underwater vehicles capitalizing on the air lubrication mechanism.

**Index Terms**—3-D dynamic modeling, air lubrication system, motion control, robotic penguin.

## I. INTRODUCTION

AFTER millions of years of natural selection, aquatic animals possess superior propulsion characteristics including high efficiency, low noise, excellent maneuverability, etc. [1]. According to the motion mechanism, it can be divided into the body and/or caudal fin (BCF) mode propelled by a flexible body like dolphin, the median and/or paired fin (MPF) mode propelled by pairs of powerful wings like manta, and the jet propulsion mode like jellyfish. These supernatural craftsmanships have motivated scientists and engineers to design various

bionic aquatic robots such as robotic dolphin [2], [3], manta [4], [5], and jellyfish [6], [7].

Over the past decades, the diving bird penguins, which have already adapted to underwater swimming and lost the capacity for flight, can utilize the burst swimming strategy of hydrofoil-like wings to achieve an unpowered gliding mode for long-distance travel. Meanwhile, the mechanism of penguins jumping out of the water onto the ice has attracted much attention from researchers. The main source has been revealed that penguins dive with compressive air in their feathers, and release during ascending [8]. The expanding microbubbles form a smooth lubrication coat over the body making it swim twice as fast as normal [9], [10]. In the engineering realm, the aforementioned method is known as bubble drag reduction (BDR). It mainly focuses on skin friction contributing up to 80% of the total drag at a slower speed. Moreover, the underlying mechanism is still an active research topic, and the main factors include the reduction in density and viscosity of the liquid, interaction with turbulent flow, dynamics of the compressive bubbles, etc. [11]. Toward BDR with actively releasing bubbles, the drag-reducing effect has been tested in the ship. Sanders *et al.* [12] investigated the high-Reynolds skin-friction drag reduction phenomenon through shear stress measurement device and bubble images, in which the drag reduction derived from the near-wall void fraction was tested. Mäkiharju *et al.* [13] established an energy economic equation based on a hypothetical air-lubricated ship and calculated that the BDR device could save 10%–20% of net energy, which would be a great achievement in navigation. Silverstream company developed a practical system to reduce the skin friction by injecting air into the bottom of the ship, and the results showed a wide application prospect [14].

The kinematics of penguin swimming have been revealed from multiple dimensions, in which the speed can be modulated from the strike frequency and amplitude, and the orientation can be empowered by the tail, feet, and wings. Unlike the thrust only renders from the downstroke of other birds' wingbeat, the thrust of the penguin can be produced from both halves of the wing-flapping cycle, close to MPF mode [15]–[18]. The aforementioned characteristics promote the study of closing the gap between the capabilities seen in nature with the robotic penguin. Remarkably, the research on the robotic penguin can be traced back to ten years ago, "AquaPenguin" which was developed by FESTO [19]. Especially, to realize the flexible motion, an innovative 3-D Fin Ray structure was equipped, and a spherical shoulder joint with a flapping mechanism was installed. By combining with intelligent sensors, navigation, collision

Manuscript received 6 October 2021; revised 7 January 2022 and 19 March 2022; accepted 24 April 2022. Date of publication 11 May 2022; date of current version 16 November 2022. This work was supported by the National Natural Science Foundation of China under Grant U1909206, Grant T2121002, Grant 61725305, Grant 61903007, and Grant 62003008. (Corresponding author: Junzhi Yu.)

Jie Pan, Ziye Zhou, and Junzhi Yu are with the State Key Laboratory for Turbulence and Complex Systems, Department of Advanced Manufacturing and Robotics, BIC-ESAT, College of Engineering, Peking University, Beijing 100871, China (e-mail: panjie@pku.edu.cn; zhouziye@pku.edu.cn; junzhi.yu@ia.ac.cn).

Jian Wang and Pengfei Zhang are with the State Key Laboratory of Management and Control for Complex Systems, Institute of Automation, Chinese Academy of Sciences, Beijing 100190, China, and also with the School of Artificial Intelligence, University of Chinese Academy of Sciences, Beijing 100049, China (e-mail: jianwang@ia.ac.cn; zhang-pengfei2017@ia.ac.cn).

This article has supplementary material provided by the authors and color versions of one or more figures available at <https://doi.org/10.1109/TIE.2022.3172753>.

Digital Object Identifier 10.1109/TIE.2022.3172753

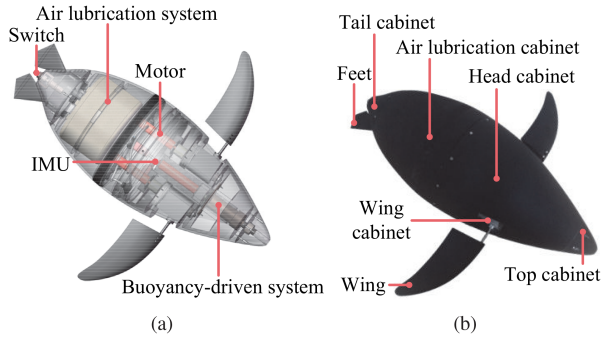


Fig. 1. Illustration of the robotic penguin. (a) Conceptual design. (b) Robotic prototype.

avoidance, depth control, etc. could be achieved. Besides, inspired by the agile wings of the penguin, Shen *et al.* [20] designed a penguin-wing-like propeller integrating flapping with feathering motions, and verified multiple performances.

The main objective of this article is to propose an innovative robotic penguin for underwater 3-D motion with an air lubrication system. The main contributions are twofold. On the one hand, a robotic penguin prototype is designed and implemented via mimicking a penguin, in which the wings have two degrees of freedom (DOF) including heaving and pitching motions to achieve flexible planar movement. Meanwhile, a buoyancy-driven system is equipped to realize decoupled Z-direction motion. Besides, a complete 3-D dynamic model capable of multimodel motions is established, and the hydrodynamic coefficients are obtained through parameter identification. On the other hand, to the best of our knowledge, it is the first time that the air lubrication system inspired by the BDR phenomenon of penguins jumping out of the water is employed on bionic aquatic robots. In particular, the superiority of the system is experimentally analyzed in different scenarios. Further, the obtained results demonstrate the universality and the maneuverability of the developed robotic penguin, which provides a reference for the biomimetic underwater robots.

The rest of this article is organized as follows. The prototype of the robotic penguin is described in Section II. The dynamic model is shown in Section III. The detailed experimental analyses are offered in Section IV. Finally, Section V concludes the article.

## II. MECHATRONIC DESIGN OF THE ROBOTIC PENGUIN

### A. Biomimetic Robotic Penguin Design

The conceptual design and prototype of the robot based on biological penguin are depicted in Fig. 1, and the corresponding specifications are tabulated in Table I. In particular, a well-streamlined body is designed for better hydrodynamic performance, and can be divided into four parts including a head cabinet containing a buoyancy-driven system, a pair of wing outer cabinets, an air lubrication cabinet, and a tail cabinet with a pair of feet.

Especially, the wings have 2-DOF movement capability including heaving and pitching motion. The heaving motion is

TABLE I  
TECHNICAL PARAMETERS OF THE ROBOTIC PENGUIN

Item	Characteristic
Size	$\sim 0.71 \times 0.66 \times 0.26 \text{ m}^3$
Total mass	$\sim 19.4 \text{ kg}$
Number of the DOF	5
Drive mode	DC motors, digital servomotors
Controller	STM32F407 (ARM based)
Power supply	DC 24 V
Communication unit	RF200 (433 MHz)
Operation time	$\sim 3 \text{ h}$

empowered by a direct current (dc) motor that mainly generates power through the reversed Karman vortex street, while the pitching motion is rendered by a digital servomotor that mostly controls the planar motion. Meanwhile, it can generate a pitch moment to realize the diving and ascending motion by adjusting the offset angle of the heaving direction on both sides. However, the strong coupling between the 2-DOF wings will greatly increase the difficulty of control for flexible 3-D motion. Thus, a buoyancy-driven system composed of a water injector and a piston is equipped to realize ascending and diving motion. The decoupling effect of the buoyancy-driven system has the ability to reduce control complexity, and the robot is designed with almost complete symmetry to provide better stability in complex scenario. Besides, inspired by the air lubrication mechanism of penguins jumping out of the water, in which the drag reduction layer originates from releasing the collecting air within a fine downy mesh in the feathers, we put forward a unique air lubrication system with a maximum pressure of 3 MPa.

### B. Construction of the Air Lubrication System

The main principle of the air lubrication system is to generate stable bubbles around the body through spraying air, thereby reducing the skin friction and increasing the speed. The details are illustrated in Fig. 2, in which the air lubrication system can be divided into three parts: 1) compressed gas cylinder (e); 2) air control unit; and 3) cabinet shell. The compressed gas cylinder (e) with approximately 2.5 L volume is used to store compressed gas. The air control unit is equipped for transporting compressed air, including solenoid valve (g) for opening and closing the system, tee fittings (c) and cross fittings (d) for air distribution, right angle adapters (f) for changing direction, polyamide (PA) pipe (j) for transmitting compressed air, flow valve (k) for controlling flow capacity, and one-way valves (i) for preventing water from flowing backward. The cabinet shell is made of nylon material and molded by 3-D printing, including the screwed joint (a) for connecting the joint of the one-way valve (i), the inclined hole with 1 mm aperture, and the cavity with 1 mm thickness (b). Notably, to avoid affecting the reversed Karmen vortex street caused by wings motion, the air lubrication system cannot be employed on the whole body like biological penguins. Thus, it is designed near the largest cross-section of the middle and rear part for the purpose of making the bubbles cover a larger area.

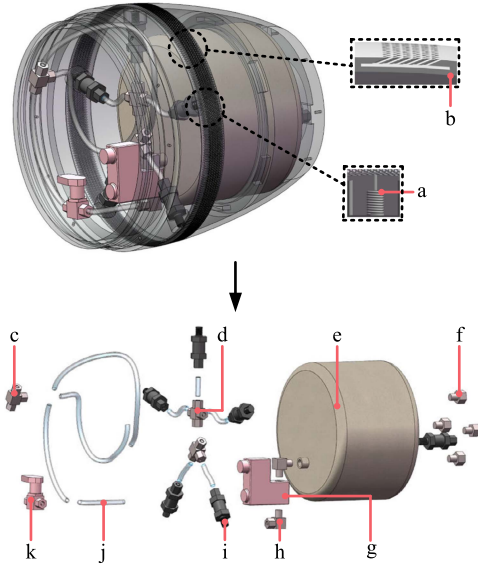


**Fig. 2.** Schematic diagram of the air lubrication system. (a) Screwed joint. (b) Inclined hole and cavity. (c) Tee fitting. (d) Cross fitting. (e) Compressed gas cylinder. (f) Attachment screw. (g) Solenoid valve. (h) Right angle adapter. (i) One-way valve. (j) PA pipe. (k) Flow valve.

The operation of the air lubrication system is divided into two stages. The first one is the air storage stage. Unlike ships that can continuously obtain air [14], the air lubrication system based on the robotic penguin needs an air compressor to pump compressed air into the cylinder (e) in advance, which is fixed with the cabinet shell by four attachment screws (f). Besides, to avoid air leakage, a one-way valve (i) is required to connect the compressed gas cylinder (e) with air compressor. The second one is the air releasing stage. Firstly, the microcontroller unit (MCU) sends an opening signal to the solenoid valve (g), the pipeline is turned ON, and the compressed air in the compressed gas cylinder (e) is delivered to the five outlets through the air control unit. Then, the air transits through the cavity (b) and is released from the inclined hole. Finally, by sending a closing signal through the MCU, the pipeline will be closed immediately.

### III. DYNAMIC MODELING

#### A. Coordinate Frames and Notation

The coordinate frames following the right-hand rule are illustrated in Fig. 3(a). The inertia frame is denoted as  $C_g = o_g x_g y_g z_g$ , and the body frame is expressed as  $C_b = o_b x_b y_b z_b$ . Meanwhile, the fin-fixed frames are defined as  $C_l = o_l x_l y_l z_l$  and  $C_r = o_r x_r y_r z_r$ . As the wings on both sides are symmetrically completed, only the right one is demonstrated in Fig. 3(b). Especially, the angle between  $o_b y_b$  and  $o_r y_r$  is expressed as  $\phi_r$ , while the angle around the  $o_r y_r$  axis is expressed as  $\theta_r$ .

The following notation convention will be utilized throughout the mathematical expressions.  ${}^i\mathbf{R}_j$  and  ${}^i\mathbf{P}_j$  denote the rotation and position matrix of  $C_j$  with respect to (w.r.t.)  $C_i$ . The cross product of  $\mathbf{p}$  and  $\mathbf{q}$  is expressed as  $\mathbf{p} \times \mathbf{q} = \hat{\mathbf{p}}\mathbf{q}$ , where  $\hat{\mathbf{p}}$  represents the skew matrix of  $\mathbf{p}$ . Furthermore, we define  $\mathbf{i} = [1, 0, 0]^T$ ,

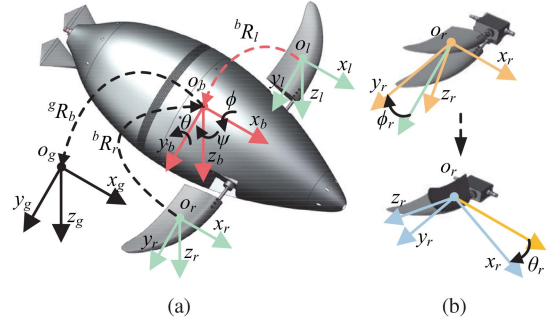


**Fig. 3.** Illustration of the symbol specification. (a) Coordinate frames. (b) Wing motion.

$$\mathbf{j} = [0, 1, 0]^T, \mathbf{k} = [0, 0, 1]^T, \mathbf{I} = [\mathbf{0}_{1 \times 3}, \mathbf{i}^T]^T, \mathbf{J} = [\mathbf{0}_{1 \times 3}, \mathbf{j}^T]^T, \text{ and } \mathbf{K} = [\mathbf{0}_{1 \times 3}, \mathbf{k}^T]^T.$$

#### B. Kinematic Analysis

The velocity vector of the robotic penguin is defined as  $\mathbf{V}_b = (\mathbf{U}_b^T, \mathbf{\Omega}_b^T)^T$ , where  $\mathbf{U}_b$  is the linear velocity and  $\mathbf{\Omega}_b$  is the angular velocity. Thus, the kinematics of the robotic penguin can be formalized by

$$\begin{aligned} {}^g\mathbf{V}_b &= {}^g\mathbf{H}_b \mathbf{V}_b \\ \mathbf{V}_i &= {}^i\mathbf{H}_b (\mathbf{V}_b + \dot{\phi}_i \mathbf{i}) + \dot{\theta}_i \mathbf{J} \quad (i = l, r) \end{aligned} \quad (1)$$

where

$$\begin{aligned} {}^g\mathbf{H}_b &= \begin{pmatrix} {}^g\mathbf{R}_b & \mathbf{0}_{3 \times 3} \\ \mathbf{0}_{3 \times 3} & {}^g\mathbf{R}_b \end{pmatrix} \\ {}^i\mathbf{H}_b &= \begin{pmatrix} {}^i\mathbf{R}_b & -{}^i\mathbf{R}_b {}^b\hat{\mathbf{P}}_i \\ \mathbf{0}_{3 \times 3} & {}^i\mathbf{R}_b \end{pmatrix} \quad (i = l, r). \end{aligned} \quad (2)$$

Especially, the attitude of the robotic penguin is parameterized by the Euler angles, and the rotation matrix can be calculated as

$$\begin{aligned} {}^g\mathbf{R}_b &= \mathbf{R}_z(\psi) \mathbf{R}_y(\theta) \mathbf{R}_x(\phi) \\ {}^i\mathbf{R}_b &= \mathbf{R}_y(-\theta_i) \mathbf{R}_x(-\phi_i) \quad (i = l, r) \end{aligned} \quad (3)$$

where  $\psi$ ,  $\theta$ , and  $\phi$  denote yaw angle, pitch angle, and roll angle, respectively.

#### C. Hydrodynamic Analysis

Hydrodynamic force can be divided into two parts: 1) the interaction between liquid and rigid body, which mainly produces resistance; 2) the interaction between liquid and wings, which mainly produces thrust. In particular, to avoid complicated calculations, the liquid is considered to be irrotational and incompressible.

We first analyze the hydrodynamic force caused by the rigid body including drag force, lift force, and moment

$$\begin{aligned} \mathbf{F}_D &= -\frac{1}{2} \rho C_D S_b \|\mathbf{U}_b\| \mathbf{U}_b \\ \mathbf{F}_L &= -\frac{1}{2} \rho C_L S_b \|\mathbf{U}_b\| \mathbf{U}_b \alpha \end{aligned}$$



$$\mathbf{M}_D = -\mathbf{C}_M \|\boldsymbol{\Omega}_b\| \boldsymbol{\Omega}_b \quad (4)$$

where  $S_b = \frac{\mathbf{U}_b^T \text{diag}\{S_x, S_y, S_z\} \mathbf{U}_b}{\|\mathbf{U}_b\|^2}$ .  $S_x$ ,  $S_y$ , and  $S_z$  denote the maximum cross section area of body in  $C_b$ ;  $\rho$  is the liquid density;  $\alpha$  indicates the angle of attack; and  $\mathbf{C}_i$  ( $i = D, L, M$ ) represents the hydrodynamic coefficients.

Given the separated flow of wings flapping motion, the simplified quasi-steady hydrodynamics is not suitable for modeling, in which the influence of acceleration cannot be ignored [21]. Thus, the Morrison equation, which is commonly used in the unsteady scenario, is employed to analyze the hydrodynamic force of wings [22]. Besides, compared with the wing area perpendicular to the Z-axis, its thickness can be neglected. Therefore, only the normal component is considered.

As the wings on both sides are symmetrically completed, only the right one is demonstrated. In particular, to facilitate the analysis, the 2-DOF motions of the wings are analyzed separately. Therefore, the hydrodynamic force can be expressed as

$$\begin{aligned} {}^r\mathbf{F}_{Hp,r} &= -\left(\rho c_{ap,r} \ddot{\theta}_r V \kappa_{1,r} + \frac{1}{2} \rho c_{dp,r} \left|\dot{\theta}_r\right| \dot{\theta}_r \kappa_{2,r}\right) \mathbf{k} \\ {}^r\mathbf{F}_{Hh,r} &= -\left(\rho c_{ah,r} \ddot{h}_r V \kappa_{1,r} |\cos(\theta_r)| \right. \\ &\quad \left. + \frac{1}{2} \rho c_{dh,r} \left|\dot{h}_r\right| \dot{h}_r \kappa_{2,r} \cos^2(\theta_r)\right) \mathbf{k} \\ {}^r\mathbf{F}_{Hb,r} &= -\rho c_{ab,r} ({}^r\dot{\mathbf{U}}_b)_z V - \frac{1}{2} \rho c_{db,r} |({}^r\mathbf{U}_b)_z| ({}^r\mathbf{U}_b)_z A \end{aligned} \quad (5)$$

where  $\mathbf{F}_H$  represents the hydrodynamic force;  $V$  is the volume of the wings;  $A$  is the cross-sectional area of the wings perpendicular to the flow;  $c_a$  denotes the inertia coefficients;  $c_d$  represents the drag coefficients;  $\kappa_1$  and  $\kappa_2$  denote the center of mass (C.M.) coordinates around their respective axes of rotation;  $\kappa_2$  and  $\kappa_2$  represent the moment of inertia; and the subscripts  $p, h, b$  are corresponded to pitching, heaving, and body motion, respectively. Besides, the influence of airfoil is simplified as an additional term which is described as

$${}^r\mathbf{F}_{A,r} = \frac{1}{2} \rho c_{a,r} \dot{\phi}_r^2 A |\cos(\theta_r)| \beta ({}^r\mathbf{R}_b \mathbf{i}) \quad (6)$$

where  $\beta$  is the airfoil angle. Specially, the moment of wings caused by hydrodynamic force is ignored.

#### D. Model Formulation

Except for hydrodynamics, the main external force is the net buoyancy, which represents the difference between gravity and buoyancy. Considering that the wing and piston accounts for a small proportion of the whole body, the C.M. of the robotic penguin are assumed stationary. Note that when the piston is at the middle position of the water injector, the net buoyancy is zero. Therefore, the net buoyancy of the robot w.r.t.  $C_b$  is given by

$$\mathbf{F}_n = -\rho S_w \left(\frac{h_m}{2} - h\right) g ({}^b\mathbf{R}_g \mathbf{k}) \quad (7)$$

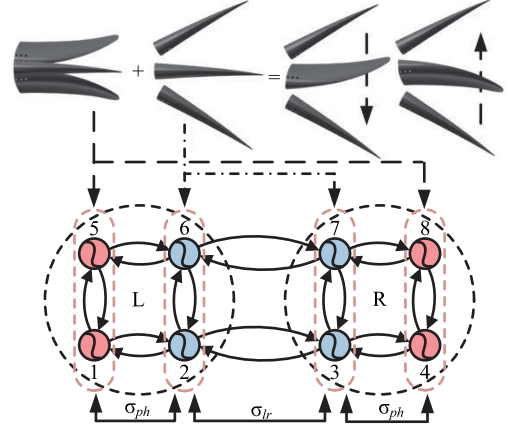


Fig. 4. Schematics of wings motion based on CPGs.

where  $g = 9.8 \text{ m/s}^2$  is the gravitational acceleration,  $S_w$  indicates the bottom area of the water injector, and  $h$  and  $h_m$  denote the position and the maximum displacement of piston. Hence, the moment of net buoyancy  $\mathbf{F}_n$  can be obtained by

$$\mathbf{M}_n = \rho S_w h g ({}^b\mathbf{R}_g \mathbf{k})^T \mathbf{P}_{in} - m_b g ({}^b\mathbf{R}_g \mathbf{k})^T \mathbf{P}_b \quad (8)$$

where  $m_b$  is the mass of body excluding the water injector, and  $\mathbf{P}_b$  and  $\mathbf{P}_{in}$  are the position vectors of corresponding center of buoyancy (C.B.) w.r.t. frame  $C_b$ . Specially, the  $\mathbf{M}_n$  is equal to zero when  $h = \frac{h_m}{2}$ .

Finally, according to the Newton–Euler equation, the dynamic model of the robotic penguin can be expressed as

$$\begin{cases} \dot{\mathbf{U}}_b = \frac{\sum_{i=L,R} {}^i\mathbf{F}_{H,i} + \mathbf{F}_n + \mathbf{F}_D + \mathbf{F}_L - m \hat{\boldsymbol{\Omega}}_b \mathbf{U}_b}{m} \\ \dot{\boldsymbol{\Omega}}_b = \mathbf{J}^{-1} \left( \sum_{i=L,R} {}^i\mathbf{M}_{H,i} + \mathbf{M}_D + \mathbf{M}_n - \hat{\boldsymbol{\Omega}}_b \mathbf{J} \boldsymbol{\Omega}_b \right) \end{cases} \quad (9)$$

where

$$\begin{cases} {}^i\mathbf{F}_{H,i} = {}^b\mathbf{R}_i ({}^i\mathbf{F}_{Hp,i} + {}^i\mathbf{F}_{Hh,i} + {}^i\mathbf{F}_{Hb,i} + {}^i\mathbf{F}_{A,i}) \\ {}^i\mathbf{M}_{H,i} = -\hat{\mathbf{P}}_i {}^i\mathbf{F}_{H,i} \end{cases} \quad (10)$$

and  $\mathbf{J} = \text{diag}(J_x, J_y, J_z)$  denotes the inertia matrix.

#### E. Basic Motion Strategy

Compared with the traditional sinusoidal signal, a stable phase relationship is generated from the central pattern generators (CPGs) through phase lag and lock, which can realize multiple behaviors of the vertebrates, invertebrates, and robots [23]. Thus, the wings motion is based on a Kuramoto phase oscillator shown in Fig. 4 to smooth abrupt state caused by strategy switching [24]

$$\begin{cases} \dot{\gamma}_i = 2\pi\nu_i + \sum_{j \in T(i)} \chi_{ij} \sin(\gamma_j - \gamma_i - \sigma_{ij}) \\ \zeta_k = 0.5(\lambda_k + \delta_k) \\ \zeta_{k+4} = 0.5(\lambda_k - \delta_k) \\ \dot{\eta}_i = \nu_i \left( \frac{\zeta_i}{4} (\zeta_i - \eta_i) - \dot{\eta}_i \right) \\ x_i = \eta_i (1 + \cos(\gamma_i)) \\ y_k = x_k - x_{k+4} \end{cases} \quad (11)$$

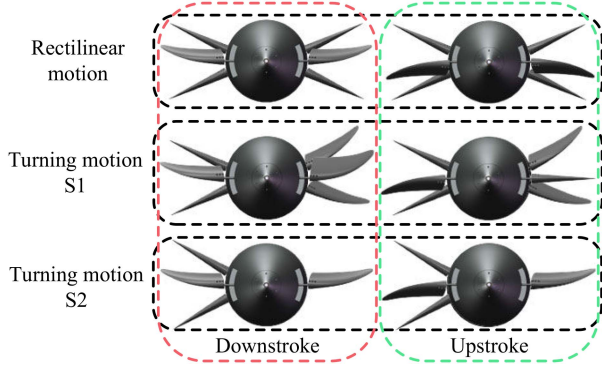


Fig. 5. Schematics of motion strategy when  $\nu = 2.0$  Hz,  $\lambda_\phi = 25^\circ$ ,  $\lambda_\theta = 30^\circ$ , and  $\delta_\theta = 30^\circ$ . (S1) Both sides of the wings maintain the rectilinear mode, in which one side rotates  $\delta_\theta$ . (S2) One side of the wings rotates  $\delta_\theta$  to remain motionless, and the other side maintains the rectilinear mode.

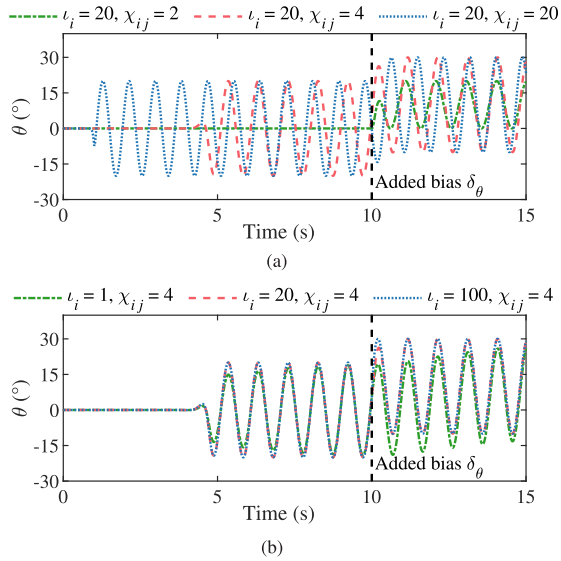


Fig. 6. Effects of CPGs parameters on wing motion where  $\lambda_\theta = 20^\circ$  and  $\delta_\theta = 10^\circ$ .

where  $i \in \{1, \dots, 8\}$ ,  $k \in \{1, \dots, 4\}$ ,  $\gamma_i$  and  $\eta_i$  indicate the phase and amplitude of the  $i$ th oscillator,  $\nu_i$  and  $\zeta_i$  determine the intrinsic frequency and amplitude,  $\chi_{ij}$  and  $\sigma_{ij}$  express the weights and phase biases between oscillators,  $\iota_i$  is a positive constant,  $\lambda_k$  and  $\delta_k$  denote the desired amplitude and offset angle,  $y_k$  is the output angle,  $T(i)$  is the set of neurons that emit coupling signals to the  $i$ th neuron, and the motion of each joint is driven by two coupled oscillators. In addition, as shown in Fig. 6, the  $\chi_{ij}$  is connected to convergence speed. The motion will deviate from the defined period if  $\chi_{ij}$  is too large, and it will be impossible to form if  $\chi_{ij}$  is too tiny. Meanwhile, the  $\iota_i$  is linked to the amplitude of convergence. The greater the  $\iota_i$  in a bias command, the more severe the state transition, and the smaller the  $\iota_i$ , the longer the state transition takes. Thus, CPG parameters were empirically selected as follows:  $\iota_i = 20$ ;  $\chi_{ij} = 4$ .

The phase biases between pitching and heaving motion  $\sigma_{ph}$  is  $\frac{\pi}{2}$  [25]. According to the establishment of  $C_l$  and  $C_r$ , the phase biases of pitching motion between the left and right side  $\sigma_{lr}$  is

TABLE II  
PARAMETER VALUES FOR THE MODEL SIMULATION

Parameters	Value	Parameters	Value
$S$	$\text{diag}(0.05, 0.12, 0.12) \text{ m}^2$	$h_m$	0.035 m
$J$	$\text{diag}(0.05, 0.17, 0.16) \text{ kg} \cdot \text{m}^2$	$m_b$	19.375 kg
$C_D$	$\text{diag}(0.9, 0.9, 0.9)$	$\beta$	$35^\circ$
$C_L$	$\text{diag}(1.15, 1.15, 1.15)$	$A$	0.012 $\text{m}^2$
$C_M$	$\text{diag}(0.14, 0.14, 0.14)$	$S_w$	$7.1 \times 10^{-4} \text{ m}^2$
$\kappa_{1,i}$	0.03 m	$\kappa_{2,i}$	$3.1 \times 10^{-5} \text{ m}^4$
$\varkappa_{1,i}$	0.147 m	$\varkappa_{2,i}$	$3.9 \times 10^{-4} \text{ m}^4$
$c_{ap,i}$	9.5	$c_{dp,i}$	1.1
$c_{ah,i}$	0.5	$c_{dh,i}$	0.2
$c_{ab,i}$	0.11	$c_{db,i}$	4
$c_{a,i}$	0.08	$\rho$	998.2 $\text{kg/m}^3$
$V$	$1.5 \times 10^{-4} \text{ m}^3$	$g$	9.8 $\text{m/s}^2$

$\pi$ . Besides, there are two turning schemes shown in Fig. 5. The one (S1) is that both sides of the wing maintain the rectilinear mode, in which one side rotates  $\delta_\theta$ , and then the turning motion is realized by the difference in thrust on both sides. The other (S2) is that the wing on one side rotates  $\delta_\theta$  to remain motionless, and the other side maintains the rectilinear mode to realize turning motion.

#### IV. EXPERIMENTS AND ANALYSIS

To evaluate the effectiveness of the developed dynamic model and the multidimensional performance of the designed robotic penguin, systematic tests were conducted in a  $5 \times 4 \times 1.5$  m experimental tank.

##### A. Model Parameter Determination

The parameters to be determined are mainly divided into two categories: 1) structural parameters and 2) hydrodynamic coefficients. In particular, the structural parameters such as the moment of inertia, the center of mass, area, and volume of each component can be measured from the SolidWorks model as shown in Fig. 1. As for the unknown hydrodynamic coefficients, the least square method is used to find the optimal solution with the least deviation between the simulation and the experimental results [26], including the maximum forward speed, maximum angular velocity, maximum ascending velocity, and maximum diving velocity. To improve the convergence speed of the algorithm, some assumptions in line with the actual situation are proposed, such as the left and right wings hydrodynamic coefficients are identical considering the identity of the geometric configuration, material structure, and motion strategy [27]. Consequently, the identified hydrodynamic parameters are shown in Table II, in which  $i$  denotes  $r$  and  $l$ .

##### B. Rectilinear Motion

To demonstrate the rectilinear motion performance of the designed robotic penguin, we explore the relationship between forward speed and three variables, in which the motion frequency was changed every 0.5 Hz from 0.5 to 1.5 Hz, the pitching amplitude was changed every  $15^\circ$  from  $0^\circ$  to  $30^\circ$ , the heaving amplitude was  $0^\circ$ ,  $10^\circ$ , and  $25^\circ$ . The experiment started with the

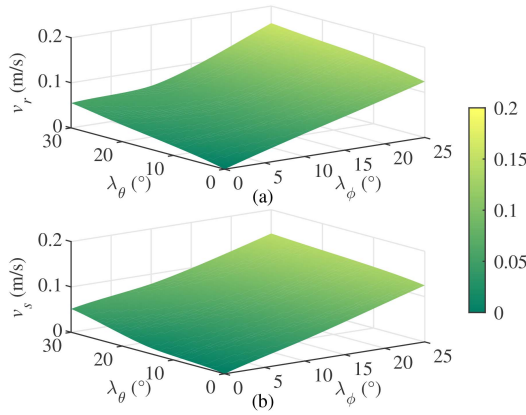


Fig. 7. Comparison of experimental and simulated forward speed for different  $\lambda_\phi$  and  $\lambda_\theta$  at  $\nu = 0.5$  Hz. (a) Experimental results. (b) Simulated results.

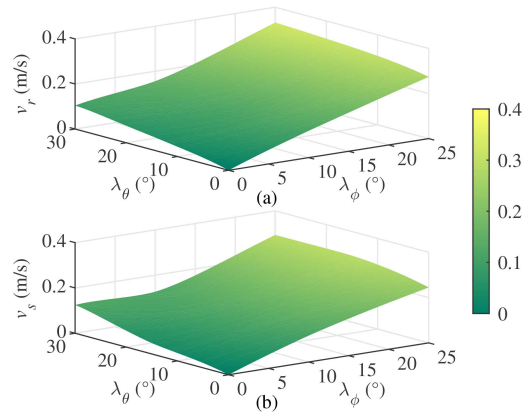


Fig. 8. Comparison of experimental and simulated forward speed for different  $\lambda_\phi$  and  $\lambda_\theta$  at  $\nu = 1.0$  Hz. (a) Experimental results. (b) Simulated results.

robotic penguin suspended at a certain point until the motion stabilized, and the global camera mounted on the top simultaneously recorded the movement data. The experimental results show that with the increase of frequency, heaving amplitude, and pitching amplitude, the forward speed is faster within the range of the parameters. The appealing phenomenon is that compared to the heaving amplitude and pitching amplitude, the frequency has a greater impact. In particular, the maximum stable speed reaches 0.567 m/s when  $\nu = 2.0$  Hz,  $\lambda_\phi = 25^\circ$ , and  $\lambda_\theta = 30^\circ$ .

Figs. 7–9 show the comparison between the simulated and experimental forward speeds, in which the normalized mean square error (NMSE) and normalized standard deviation (NSD) are 0.1527 and 0.1616, respectively. The fitting indicators verify the effectiveness of the dynamic model.

### C. Vertical Motion

In this section, we focus on the role of the buoyancy-driven system in ascending and diving. In particular, the maximum displacement of the piston is 0.07 m, and the yield net buoyancy range is 0.242 N. Through experiments in the pool, the maximum stable vertical velocity of ascending is 0.03 m/s, the maximum

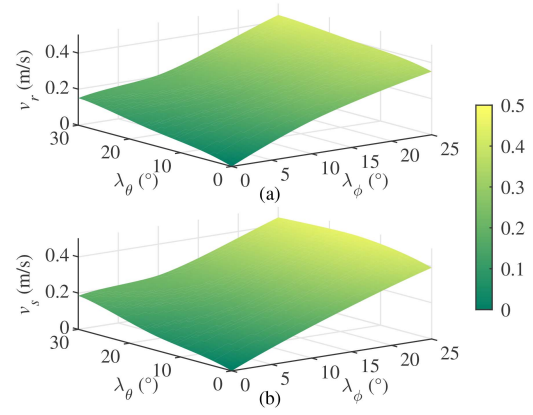


Fig. 9. Comparison of experimental and simulated forward speed for different  $\lambda_\phi$  and  $\lambda_\theta$  at  $\nu = 1.5$  Hz. (a) Experimental results. (b) Simulated results.

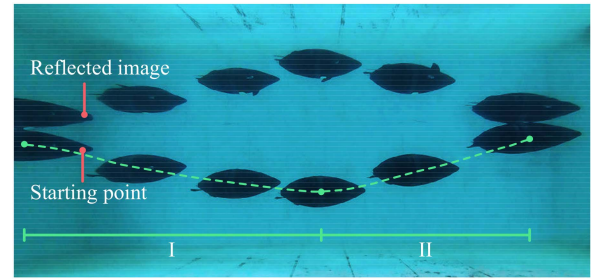


Fig. 10. Snapshots of the robotic penguin during ascending and diving motion at  $\nu = 0.5$  Hz,  $\lambda_\phi = 10^\circ$ , and  $\lambda_\theta = 30^\circ$ .

stable vertical velocity of diving is 0.06 m/s, and the corresponding simulated velocity is 0.031 m/s and 0.040 m/s, respectively. The difference between ascending and diving velocity is mainly due to the counterweights and lift-to-drag ratios. Besides, the snapshots of vertical motion are shown in Fig. 10, where the upper part is the inverted image of the water surface, segment I is diving, and segment II is ascending.

### D. Turning Motion

For evaluating turning performance, there are two main indicators, angular velocity  $\omega$  and turning radius  $r$ , which can be calculated by the global vision system with red and yellow color blocks. Especially, the position information of red and yellow blocks can be observed by the identification algorithm, and the yaw angle of the robotic penguin w.r.t. the  $C_g$  can be obtained. In addition, to calculate the turning radius  $r$ , the center of the yellow color block is regarded as the C.M., which is consistent with the physical situation. Therefore, the angular velocity  $\omega$  can be determined based on the time and yaw angle between the two images, while the turning radius  $r$  can be acquired by the trajectory of the yellow color block.

Fig. 11 shows the comparison between two turning strategies, in which the  $\delta_\theta$  was changed every  $30^\circ$  from  $0^\circ$  to  $90^\circ$ . In particular, for S1,  $\delta_\theta = 0^\circ$  means swimming forward, which is out of the scope of the discussion. In addition, it is obvious that the greater the thrust, the larger the steering moment



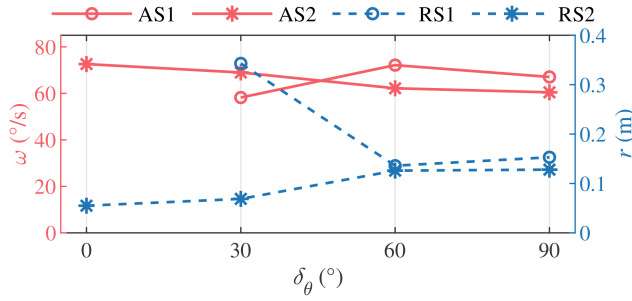


Fig. 11. Comparison of different turning strategies when  $\nu = 2.0$  Hz,  $\lambda_\phi = 25^\circ$ , and  $\lambda_\theta = 30^\circ$ . (AS1) The angular velocity  $\omega$  under S1. (AS2) The angular velocity  $\omega$  under S2. (RS1) The turning radius  $r$  under S1. (RS2) The turning radius  $r$  under S2.



Fig. 12. Snapshots of the robotic penguin during turning motion with S2 at  $\delta_\theta = 0^\circ$ ,  $\nu = 2.0$  Hz,  $\lambda_\phi = 25^\circ$ , and  $\lambda_\theta = 30^\circ$ .

generated by the offset  $\delta_\theta$ . Thus, the motion parameters were set as  $\nu = 2.0$  Hz,  $\lambda_\phi = 25^\circ$ , and  $\lambda_\theta = 30^\circ$  to search maximum angular velocity  $\omega$ .

Through average filtering, the maximum angular velocity obtained by S1 is  $72.155^\circ/\text{s}$  in  $\delta_\theta = 60^\circ$ , and the maximum angular velocity obtained by S2 is  $72.605^\circ/\text{s}$  in  $\delta_\theta = 0^\circ$ , in which the corresponding turning radius is 0.14 and 0.06 m, respectively. Besides, the snapshots of turning motion with S2 are demonstrated in Fig. 12, and the yellow line draws the trajectory of the yellow block for calculating the turning radius. According to the monotonicity of the S2, the angular velocity  $\omega$  decreases with the increase of  $\delta_\theta$ . It is caused by the reverse steering torque induced from the increased waterfront area. On the contrary, the S1 curve performs nonmonotonicity, which is mainly caused by three factors in the following aspects.

- 1) The biased side wing that maintains the rectilinear mode can generate thrust, which induces a reverse steering torque, and the larger the  $\delta_\theta$ , the smaller the reverse steering torque with the greater the  $\omega$ .
- 2) The biased side wing that maintains the rectilinear mode can generate lift, which reduces the roll angle that produces the resistance when turning, and the larger the  $\delta_\theta$ , the greater the roll angle with the smaller the  $\omega$ .
- 3) As the  $\delta_\theta$  increases, the waterfront area increases, and the reverse steering torque brings the  $\omega$  smaller, similar to S2.

Meanwhile, as for the turning radius, S2 is better than S1, which is mainly due to the offset wing in S1 still generating thrust. Especially, the fitting effect of S1 is better than S2 in the

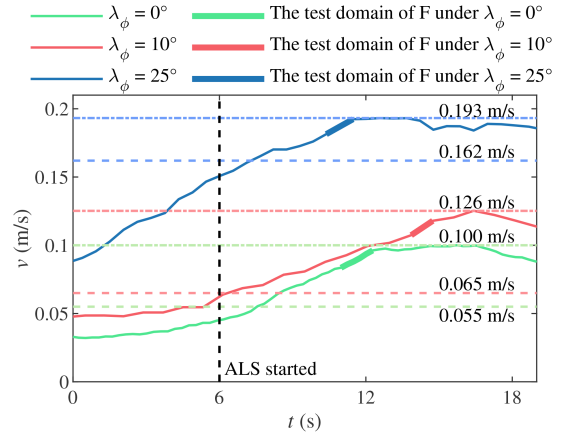


Fig. 13. Experimental results of the forward speed for different  $\lambda_\phi$  at  $\nu = 0.5$  Hz and  $\lambda_\theta = 30^\circ$  with air lubrication. (ALS) Air lubrication system. (F) Net force.

simulation, where the NMSE of S1 is 0.0617, and the NMSE of S2 is 0.5398.

### E. Performance of Air Lubrication System

Inspired by the air lubrication mechanism of the penguin jumping out of the water, the air lubrication system of the robotic penguin was already given in Section II, and its effectiveness will be discussed in the following part.

It ought to be noted that, unlike injecting compressed gas from the tail to obtain propulsion, the acceleration of BDR is a compound effect of multiple mechanisms. Therefore, to analyze the effectiveness and feasibility of the designed air lubrication system, the maximum stable speed before and after the air lubrication system was compared under the same motion conditions. Specially, the pressure of the air inside the compressed gas cylinder was 1.5 MPa.

Fig. 13 describes the forward speed of the robotic penguin when the air lubrication system is turned ON for different  $\lambda_\phi$  at  $\nu = 0.5$  Hz and  $\lambda_\theta = 30^\circ$ , which is the most intuitive experiment to reflect its effectiveness and feasibility. After average filtering, the maximum stable speed is increased from 0.055 to 0.100 m/s, 0.065 to 0.126 m/s, and 0.162 to 0.193 m/s, respectively. These experimental results show that the air lubrication system significantly improves the motion performance in the rectilinear mode.

Fig. 14 depicts the snapshots of the robotic penguin during air lubrication, in which the abundance of compressed bubbles released depends on the pressure of the remaining stored air, and the whole air lubrication system process can be divided into three periods, including the development period, the duration period, and the decline period. The development period is mainly the process of bubbles from zero to abundance, and the period is relatively short. Then, there is the duration period shown in Fig. 15, which is the main period of air lubrication. The bubbles are attached to the surface and constantly replaced by new ones. The rear section of the robotic penguin formed a smooth lubricating coat similar to that of the penguin jumping out of the water. In particular, it is also a significant acceleration

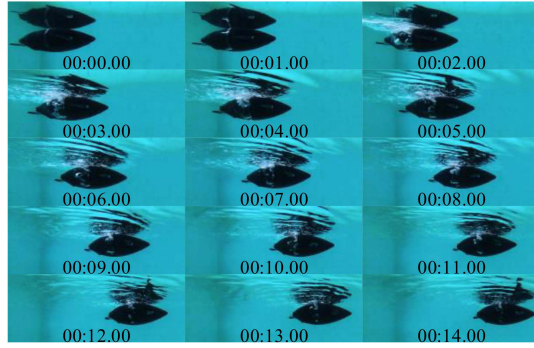


Fig. 14. Snapshots of the robotic penguin during air lubrication at  $\nu = 0.5$  Hz,  $\lambda_\phi = 0^\circ$ , and  $\lambda_\theta = 30^\circ$ .

TABLE III  
COMPARISON OF NET FORCE FOR DIFFERENT SCENARIOS

Scenario	Net Force	Improvement
Six-axis force sensor	0.152 N	-
$\nu = 0.5$ Hz, $\lambda_\phi = 0^\circ$ , $\lambda_\theta = 30^\circ$	0.190 N	25.0%
$\nu = 0.5$ Hz, $\lambda_\phi = 10^\circ$ , $\lambda_\theta = 30^\circ$	0.230 N	52.0%
$\nu = 0.5$ Hz, $\lambda_\phi = 25^\circ$ , $\lambda_\theta = 30^\circ$	0.195 N	28.3%

TABLE IV  
COMPARISON OF EXISTING UNDERWATER ROBOTS DRIVEN BY MPF

Item	Robotic manta [28]	Robotic manta [29]	Robotic manta [5]	Robotic penguin [19]	Developed robotic penguin
Length (m)	0.46	0.6	0.381	0.77	0.71
Width (m)	0.7	0.92	0.723	0.66	0.66
Weight (kg)	3.4	6.2	3.68	9.6	19.4
DOF of the wings	4	6	6	6	4
Maximum forward speed (BL/s)	0.99	0.7	1.07	1.8	0.8
Maximum angular velocity ( $^\circ$ /s)	60	36	68.9	-	72.605
Air lubrication ability	No	No	No	No	Yes

stage. Finally, there is a long-lasting recession period, when the pressure of the residual air is difficult to maintain the lubrication layer at the current speed.

The direction of the pores is set to  $70^\circ$  with the  $X$ -axis of  $C_b$  in Fig. 3, which is consistent with the liquid motion to attach more bubbles downstream of the injection port [12]. Thus, the air lubrication effect and the reaction force of the air-jet will appear. To analyze the acceleration source of the air lubrication system, the six-axis force sensor ATI-Delta IP68 is employed as an estimate of reaction force, which is shown in Figs. 16 and 17. Meanwhile, based on the momentum theorem, the experimental forward speed with air lubrication is employed to analyze the acceleration source, in which the experimental period should be after the maximum speed to reduce the influence of the wing motion. In particular, the experimental period is shown in Fig. 13, where the starting points of all periods are greater than 4 s after the air lubrication system is activated. Considering the air lubrication system is started at 5 s and the reaction force will decay over time shown in Fig. 17, the maximum fitting value at 9 s is used as the basis of reaction force. The calculated results are shown in Table IV, where the improvement results refer to the

improved effect of the air lubrication system in drag reduction, compared to the reaction force measured by the six-axis force sensor. Even if compared with the maximum value of 0.170 N after 9 s, the calculated net force is larger. In summary, the acceleration effect achieved by this system is the sum of the air lubrication effect and the reaction force of air jet.

## F. Discussion

Table IV tabulates the comparison of existing underwater robots driven by MPF, in which the body-length (BL) speed is uniformly used to evaluate the forward swimming speed of the different bionic underwater robots. In particular, the maximum stable forward speed of the robotic penguin is 0.8 BL/s, which is lower than that of FESTO [19], but it is the average level for robotic manta, which adopts MPF motion mode [5], [28], [29]. Meanwhile, due to the lack of literature on the maximum angular velocity of the robotic penguin, the typical robotic manta is selected as the control group, and the robotic penguin can reach  $72.605^\circ$ /s, which is the highest level. In summary, compared with the existing MPF-driven swimming robot, the robotic penguin designed in this article achieves an average speed level and has higher steering flexibility. Remarkably, there is a big gap between the developed robotic penguin and the biological penguins, but the study of the bionic robotic penguin can advance the exploration of the penguin motion mode.

As can be seen from Figs. 14 and 15, the air lubrication system is nontrivial in the auxiliary motion mechanism, which is rarely exploited in the robot realm. Firstly, from the perspective of mechanism, the acceleration effect is the combination of the flow compressibility from bubbles, the reduction of medium density and viscosity, the interaction of turbulence, the dynamics of compressed bubbles, etc. Secondly, according to the comparison between the lubrication coat of the biological penguins formed around the whole body, the lubrication coat of the robotic penguin consistent with the design is mainly on the second half. At the same time, the biological penguin feather is comparable to a porous medium with  $<20 \mu\text{m}$  aperture [30], making a higher bubble abundance than the robotic penguin. Then, from the form of the lubrication coat, the air lubrication system in this article is more similar to ships [14], which is also subject to physical constraints, and the wrapping phenomenon is achieved by relative motion and buoyancy. Next, the effect of the air lubrication system has been verified in other swimming modes. During the turning mode, the angular velocity will decrease, and the turning radius will increase with drift. In the ascending and diving mode, after the air lubrication system is activated, the weight of the robotic penguin is reduced, which is conducive to ascending motion. Finally, according to the air lubrication technical in the laboratory and for the full ship scales, the speed, air injection flow rate, void fraction, coverage area, etc. are related to the drag reduction effect, which is worthy for further investigation to optimize the developed air lubrication system [11]. In summary, the air lubrication system has been proved to be effective in improving the speed of the robotic penguin and can be used as an auxiliary means to enhance the performance of swimming robot in the future. Although the air lubrication system for the



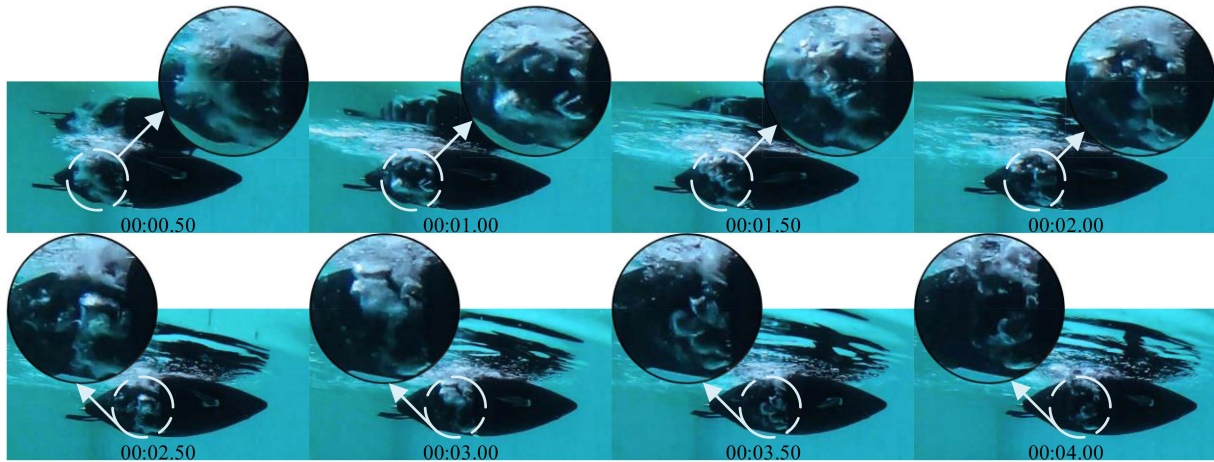


Fig. 15. Snapshots of the robotic penguin during the bubble duration stage of air lubrication at  $\nu = 0.5$  Hz,  $r_\phi = 0^\circ$ , and  $r_\theta = 30^\circ$ .

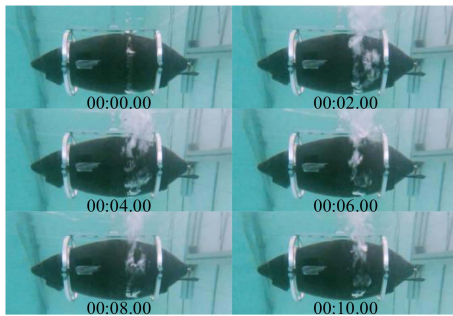


Fig. 16. Snapshots of the robotic penguin during air lubrication with the six-axis force sensor.

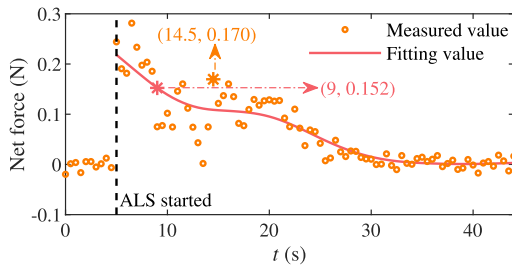


Fig. 17. Thrust of the six-axis force sensor results in a static state with air lubrication.

realization of the jumping still requires greater efforts including a more ingenious lubrication system, a greater air pressure, etc., it will serve as a benchmark for subsequent refinements.

## V. CONCLUSION

In this article, we have developed a novel penguin-inspired swimming robot with a bionic air lubrication system. Firstly, a proof-of-concept prototype was designed, including a buoyancy adjustment system, a pair of controllable wings with 2-DOF movement capability, and an air lubrication system. Secondly, based on the Morrison equation, considering gravity and buoyancy, a complete dynamic model was established, and the hydrodynamic parameters were calculated through comparison with

experimental data. Finally, we conducted a series of experimental analyses, including rectilinear swimming, turning, ascending, diving, and the effectiveness of the air lubrication system. It is worth noting that the results obtained in this article will help the innovative research of the next generation robotic penguin, and adapt to more complex scenarios, such as underwater inspections and artificial reef surveys.

In the future, we will increase the active surface area, optimize the streamlined shell curve, add wire-driven joints, etc. to improve the current robotic penguin and finally obtain the amphibious capabilities including ice sports similar to the biological penguin.

## REFERENCES

- [1] M. Triantafyllou and G. Triantafyllou, "An efficient swimming machine," *Sci. Amer.*, vol. 272, no. 3, pp. 64–70, Mar. 1995.
- [2] J. Yu, Z. Wu, Z. Su, T. Wang, and S. Qi, "Motion control strategies for a repetitive leaping robotic dolphin," *IEEE/ASME Trans. Mechatronics*, vol. 24, no. 3, pp. 913–923, Jun. 2019.
- [3] J. Wang, Z. Wu, M. Tan, and J. Yu, "3-D path planning with multiple motions for a gliding robotic dolphin," *IEEE Trans. Syst., Man, Cybern., Syst.*, vol. 51, no. 5, pp. 2904–2915, May 2021.
- [4] C. Zhou and K. Low, "Design and locomotion control of a biomimetic underwater vehicle with fin propulsion," *IEEE/ASME Trans. Mechatronics*, vol. 17, no. 1, pp. 25–35, Feb. 2012.
- [5] Y. Meng, Z. Wu, H. Dong, J. Wang, and J. Yu, "Toward a novel robotic manta with unique pectoral fins," *IEEE Trans. Syst., Man, Cybern., Syst.*, vol. 52, no. 3, pp. 1663–1673, Mar. 2022.
- [6] A. Villanueva, C. Smith, and S. Priya, "A biomimetic robotic jellyfish (Robojelly) actuated by shape memory alloy composite actuators," *Bioinspir. Biomim.*, vol. 6, no. 3, Aug. 2011, Art. no. 036004.
- [7] J. Frame, N. Lopez, O. Curet, and E. Engeberg, "Thrust force characterization of free-swimming soft robotic jellyfish," *Bioinspir. Biomim.*, vol. 13, no. 6, Sep. 2018, Art. no. 064001.
- [8] J. Davenport, R. Hughes, M. Shorten, and P. Larsen, "Drag reduction by air release promotes fast ascent in jumping emperor penguins—A novel hypothesis," *Mar. Ecol. Prog. Ser.*, vol. 430, pp. 171–182, May 2011.
- [9] K. Sato *et al.*, "Buoyancy and maximal diving depth in penguins: Do they control inhaling air volume?," *J. Exp. Biol.*, vol. 205, no. 9, pp. 1189–1197, 2002.
- [10] K. Sato, P. Pongonis, Y. Habara, and Y. Naito, "Emperor penguins adjust swim speed according to the above-water height of ice holes through which they exit," *J. Exp. Biol.*, vol. 208, no. 13, pp. 2549–2544, 2005.
- [11] S. Sindagi and R. Vijayakumar, "Succinct review of MBDR/BDR technique in reducing ships drag," *Ships Offshore Struct.*, vol. 16, no. 9, pp. 968–979, 2021.

- [12] W. Sanders, E. Winkel, D. Dowling, M. Perlin, and S. Ceccio, "Bubble friction drag reduction in a high-Reynolds-number flat-plate turbulent boundary layer," *J. Fluid Mech.*, vol. 552, pp. 353–380, Mar. 2006.
- [13] S. MäKiharju, M. Perlin, and S. Ceccio, "On the energy economics of air lubrication drag reduction," *Int. J. Nav. Archit. Ocean Eng.*, vol. 4, no. 4, pp. 412–422, Dec. 2012.
- [14] N. Silberschmidt, D. Tasker, T. Pappas, and J. Johannesson, "Silverstream system-air lubrication performance verification and design development," in *Proc. Conf. Shipp. Changing Clim.*, Newcastle, U.K., 2016, pp. 11–12.
- [15] B. Clark and W. Bemis, "Kinematics of swimming of penguins at the detroit zoo," *J. Zool.*, vol. 188, no. 3, pp. 411–428, Jul. 1979.
- [16] R. Dam, P. Ponganis, V. Ponganis, H. Levenson, and G. Marshall, "Stroke frequencies of emperor penguins diving under sea ice," *J. Exp. Biol.*, vol. 205, no. 24, pp. 3769–3774, 2002.
- [17] Y. Watanuki *et al.*, "Swim speeds and stroke patterns in wing-propelled divers: A comparison among alcids and a penguin," *J. Exp. Biol.*, vol. 209, no. 7, pp. 1217–1230, 2006.
- [18] K. Sato, K. Shiomi, G. Marshall, G. Kooyman, and P. Ponganis, "Stroke rates and diving air volumes of emperor penguins: Implications for dive performance," *J. Exp. Biol.*, vol. 214, no. 7, pp. 1217–1230, 2011.
- [19] W. Stoll, "AquaPenguin," FESTO, Esslingen, Germany, Tech. Rep. 54711/EN, 2009.
- [20] Y. Shen, N. Harada, S. Katagiri, and H. Tanaka, "Biomimetic realization of a robotic penguin wing: Design and thrust characteristics," *IEEE/ASME Trans. Mechatronics*, vol. 26, no. 5, pp. 2350–2361, Oct. 2021.
- [21] H. Taha, M. Hajj, and A. Nayfeh, "Flight dynamics and control of flapping-wing MAVs: A review," *Nonlinear Dyn.*, vol. 70, pp. 907–939, Jul. 2012.
- [22] J. Yuan, Z. Wu, J. Yu, and M. Tan, "Sliding mode observer-based heading control for a gliding robotic dolphin," *IEEE Trans. Ind. Electron.*, vol. 64, no. 8, pp. 6815–6824, Aug. 2017.
- [23] J. Yu, M. Tan, J. Chen, and J. Zhang, "A survey on CPG-inspired control models and system implementation," *IEEE Trans. Neural Netw. Learn. Syst.*, vol. 25, no. 3, pp. 441–456, Mar. 2014.
- [24] A. Crespi and A. Ijspeert, "Online optimization of swimming and crawling in an amphibious snake robot," *IEEE Trans. Robot.*, vol. 24, no. 1, pp. 751–787, Feb. 2008.
- [25] S. Licht, V. Polidoro, M. Flores, F. Hover, and M. Triantafyllou, "Design and projected performance of a flapping foil AUV," *IEEE J. Ocean. Eng.*, vol. 29, no. 3, pp. 786–794, Jul. 2004.
- [26] J. Yu, J. Yuan, Z. Wu, and M. Tan, "Data-driven dynamic modeling for a swimming robotic fish," *IEEE Trans. Ind. Electron.*, vol. 63, no. 9, pp. 5632–5640, Sep. 2016.
- [27] W. Wang *et al.*, "Three-dimensional modeling of a fin-actuated robotic fish with multimodal swimming," *IEEE/ASME Trans. Mechatronics*, vol. 23, no. 4, pp. 1641–1652, Aug. 2018.
- [28] L. Zhang, C. Niu, S. Bi, and Y. Cai, "Kinematic model analysis and design optimization of a bionic pectoral fin," in *Proc. IEEE Int. Conf. Robot. Biomimetic*, Shenzhen, China, 2013, pp. 2219–2224.
- [29] Y. Cai, S. Bi, G. Li, H. P. Hildre, and H. Zhang, "From natural complexity to biomimetic simplification: The realization of bionic fish inspired by the cownose ray," *IEEE Robot. Autom. Mag.*, vol. 26, no. 3, pp. 27–38, Sep. 2019.
- [30] N. Du, J. Fan, H. Wu, S. Chen, and Y. Liu, "An improved model of heat transfer through penguin feathers and down," *J. Theor. Biol.*, vol. 248, no. 4, pp. 727–735, Oct. 2007.



**Jie Pan** received the B.E. degree in aircraft manufacture engineering from Northwestern Polytechnical University, Xi'an, China, in 2018. He is currently working toward the Ph.D. degree in general and fundamental mechanics with the College of Engineering, Peking University, Beijing, China.

His research interests include bioinspired underwater robots, path tracking, and reinforcement learning.



**Ziye Zhou** received the B.E. degree in naval architecture and ocean engineering and the M.E. degree in design and manufacture of marine structures from Harbin Engineering University, Harbin, China, in 2016 and 2019, respectively. He is currently working toward the Ph.D. degree in general and fundamental mechanics with the College of Engineering, Peking University, Beijing, China.

His current research interests include intelligent control of bioinspired underwater robots and swarm intelligence.



**Jian Wang** (Member, IEEE) received the B.E. degree in automation from the University of Science and Technology Beijing, Beijing, China, in 2016, and the Ph.D. degree in control theory and control engineering from the Institute of Automation, Chinese Academy of Sciences (IACAS), Beijing, in 2021.

He is currently an Assistant Professor with the State Key Laboratory of Management and Control for Complex Systems, IACAS. His research interests include bioinspired underwater robots and intelligent control systems.



**Pengfei Zhang** received the B.E. degree in detection, guidance and control techniques from the School of Aeronautics and Astronautics, Central South University, Changsha, China, in 2017. He is currently working toward the Ph.D. degree in control theory and control engineering from the Institute of Automation, Chinese Academy of Sciences (IACAS), Beijing, China.

His research interests include the intelligent control and environmental perception of bioinspired robotic fish.



**Junzhi Yu** (Fellow, IEEE) received the B.E. degree in safety engineering and the M.E. degree in precision instruments and mechatronics from the North University of China, Taiyuan, China, in 1998 and 2001, respectively, and the Ph.D. degree in control theory and control engineering from the Institute of Automation, Chinese Academy of Sciences, Beijing, China, in 2003.

From 2004 to 2006, he was a Postdoctoral Research Fellow with the Center for Systems and Control, Peking University, Beijing. In 2006, he was an Associate Professor with the Institute of Automation, Chinese Academy of Sciences, where he became a Full Professor in 2012. In 2018, he joined the College of Engineering, Peking University, as a Tenured Full Professor. His current research interests include intelligent robots, motion control, and intelligent mechatronic systems.